One-magnon inelastic light scattering in the canted antiferromagnet NiF_2

E. Meloche,[1,*] M. G. Cottam,[1] V. P. Gnezdilov,[2,†] and D. J. Lockwood[2]
[1]*Department of Physics and Astronomy, University of Western Ontario, London, Ontario, Canada N6A 3K7*
[2]*Institute for Microstructural Sciences, National Research Council, Ottawa, Ontario, Canada K1A 0R6*
(Received 9 June 2009; revised manuscript received 2 November 2009; published 27 January 2010)

Experimental results concerning the temperature and polarization dependence of the one-magnon Raman light scattering in the canted antiferromagnet NiF_2 (Néel temperature T_N=73 K) are reported. The excitation frequencies, linewidths, and integrated intensities of the lower and upper magnon branches are obtained over the temperature range 5–65 K. A comparison between theory and experiment for the frequencies of the one-magnon branches shows good overall agreement for temperatures up to $0.3T_N$. A theoretical model that includes the effects of linear and quadratic magneto-optical coupling is used to account for the observed polarization characteristics of the Stokes and anti-Stokes peaks. The analysis takes account of the small canting angle of the spins which complicates the behavior of the lower magnon branch, in particular. The experimental data are indicative of a possible spin-reorientation transition at ~31 K.

DOI: 10.1103/PhysRevB.81.024426 PACS number(s): 75.50.Ee, 72.10.Di, 78.20.Ls, 78.30.−j

I. INTRODUCTION

In a recent paper[1] we reported a comparison between experiment and theory for two-magnon inelastic light scattering in the rutile-structure antiferromagnets NiF_2 and CoF_2, supplementing earlier work on other isomorphic compounds such as FeF_2 and MnF_2 that are similar magnetically.[2] Further information about the magnetic properties of these compounds can be gained from the one-magnon light scattering, which emphasizes the magnetic excitations near the Brillouin-zone center, rather than the large wave vectors involved in the two-magnon scattering. As with the two-magnon scattering,[1] it is again the case that NiF_2 and CoF_2 are not well understood with regards to both the temperature and polarization dependence of the magnon excitations, as studied through their frequencies and Raman intensities. Therefore in the present work we investigate the light-scattering properties of the one-magnon excitations in the $S=1$ antiferromagnet NiF_2 (T_N=73 K), where the spin canting from true antiferromagnetic alignment has a major influence. The one-magnon light scattering in CoF_2, which has other distinctive properties due to orbital angular momentum effects, will be the topic of a later study.

The crystallographic unit cell of NiF_2 is depicted in Fig. 1 together with the relevant exchange parameters employed in this work. It is well known (e.g., from inelastic neutron-scattering studies[3]) that the spins in NiF_2 are canted due to anisotropy effects. Specifically, the spins preferentially lie in the plane perpendicular to the c axis and are canted from antiparallel alignment by a small angle estimated to be about 0.5° at low temperatures.[3,4] The twofold degeneracy in the one-magnon spectrum is removed since the resulting small net ferromagnetic moment gives rise to an additional low-frequency magnon excitation (which depends sensitively on the canting angle) in addition to the usual higher frequency excitation observed in other antiferromagnets, such as CoF_2, MnF_2, and FeF_2,[5,6] where there is no spin canting.

Earlier one-magnon Raman experiments (see, e.g., Cottam and Lockwood[2] for a review) are extended here by providing a comprehensive study of the frequencies and intensities for both magnon branches, including the temperature and polarization dependences of the excitations. These data are then employed to carry out a theoretical analysis of the excitations and the magneto-optical coupling mechanisms. The theory is based on a Green's function equation-of-motion method, which is formally similar to that employed by Awang and Cottam[7] for other magnetic systems with single-ion anisotropy. This includes employing an Anderson-Callen[8] decoupling approximation for the higher order Green's functions involving the product of spin operators at the same site. The scattering intensities are evaluated using a spin-dependent polarizability that includes linear and quadratic magneto-optical coupling coefficients.[2] Comparisons of the theory with the experimental data for the integrated intensities of the Stokes and anti-Stokes scattering enable us to deduce information for some of the relative values of the magneto-optical coefficients. The inclusion of quadratic magneto-optical coupling is needed to explain some of the observed polarization characteristics.

We represent the spin excitations in NiF_2 using the following Hamiltonian:

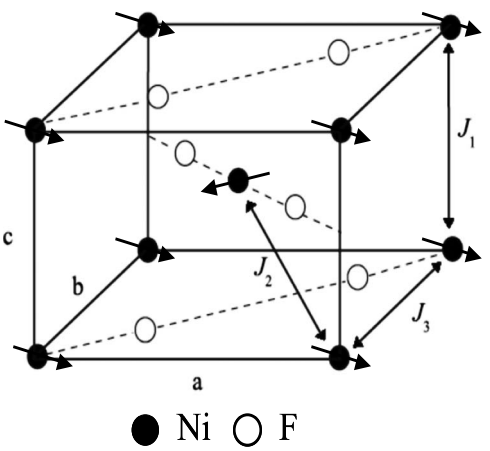

FIG. 1. The crystallographic unit cell of NiF_2 along with the dominant exchange interactions J_1, J_2, and J_3.

$$\mathcal{H} = \sum_{i,j} J_{i,j} \boldsymbol{S}_i \cdot \boldsymbol{S}_j + \frac{1}{2} \sum_{i,i'} J'_{i,i'} \boldsymbol{S}_i \cdot \boldsymbol{S}_{i'} + \frac{1}{2} \sum_{j,j'} J'_{j,j'} \boldsymbol{S}_j \cdot \boldsymbol{S}_{j'} + \sum_i \{D(S_i^z)^2 - F[(S_i^x)^2 - (S_i^y)^2]\} + \sum_j \{D(S_j^z)^2 + F[(S_j^x)^2 - (S_j^y)^2]\}, \quad (1)$$

where $J_{i,j}$ is the intersublattice antiferromagnetic exchange between sites i and j on different sublattices while $J'_{i,i'}$ and $J'_{j,j'}$ are the intrasublattice exchange interactions. The spins at sites labeled i refer to corner sites and the spins at sites labeled j represent body-centered sites of the NiF_2 tetragonal lattice. The parameters D and F describe the effects of the uniaxial and nonuniaxial contributions to the single-ion anisotropy, respectively. The x and y axes are at 45° with respect to the crystal a and b axes.[1] The parameter values (all in cm^{-1}) used in our calculations are $J_1 = -0.22$, $J_2 = 13.87$, and $J_3 = 0.79$ for the dominant exchange terms, with $D = 4.36$ and $F = 1.66$ for the anisotropy terms, following Hutchings *et al.*[3] With the exception of F, which was undetermined, these values are all consistent with Ref. 1.

In Sec. II we describe the Raman-scattering experiments and present results for the temperature and polarizations dependences of the one-magnon scattering. Then in Sec. III we describe the theoretical model and outline the calculations of the transverse spin-spin correlations functions and excitations energies. The one-magnon light-scattering cross section in the canted antiferromagnet is also calculated in Sec. III by following a standard method,[9–11] and the comparisons between theory and experiment are presented in Sec. IV. Finally Sec. V contains further discussions and the conclusions of our work.

II. EXPERIMENT AND RESULTS

The yellowish-green-colored sample of NiF_2 was prepared from a single crystal grown by B. Wanklyn and B. E. Watts at the Clarendon Laboratory, Oxford University that was especially commissioned for this study. The cuboid sample of dimensions $4.2 \times 3.7 \times 1.1$ mm^3 was cut to expose (001) [Z], (110) [X], and $(1\bar{1}0)$ [Y] faces, respectively, and these faces were highly polished with 1 μm diamond powder. The Raman spectrum was excited with 300 mW of 514.5 nm Argon ion laser light filtered by an Anaspec 300S prism monochromator. The use of green laser light minimized any sample heating due to optical absorption, especially at low temperatures. In the experiments, the incident laser light was directed quite close to the exit face of the sample (the face from which the scattered light was collected) to further reduce any possible optical-absorption effects on the scattered light intensity. The scattered light from the upper branch magnon was analyzed with a Spex 14018 double monochromator at a spectral resolution of 1.86 cm^{-1} and detected by a cooled RCA 31034A photomultiplier. The sample was mounted in the helium exchange-gas space of a Thor S500 continuous flow cryostat, where the temperature could be controlled to within 0.1 K and was measured with a gold-iron/chromel thermocouple clamped to the sample. The scattered light from the lower branch magnon was analyzed with a SOPRA DMDP double monochromator at a spectral resolution of 0.42 cm^{-1} and detected by a cooled Hamamatsu R928P photomultiplier. The sample was mounted in the helium gas space of a Janis Varitemp cryostat, where the temperature could be controlled to within 0.1 K and was measured with a gold-iron/chromel thermocouple clamped to the sample. Spectra were recorded in the 90° scattering geometry. The one-magnon scattering in both branches was measured in different polarizations for temperatures up to about T_N. All measured spectra were fitted with a Gaussian-Lorentzian line shape using the commercial curve-fitting software package PEAKFIT (Ref. 12) to extract the one-magnon band parameters of peak frequency, linewidth (full width at half maximum), and integrated intensity. For the lower branch magnon spectra, another curve-fitting software package SP2 developed at the B. I. Verkin Institute for Low Temperature Physics, National Academy of Sciences, Ukraine was also used to evaluate the one-magnon band parameters. The temperature dependence of the upper branch one-magnon scattering was also recorded in select polarizations with the SOPRA spectrometer and spectra recorded at 10.0 K were used to obtain a normalization factor of 16.91 between the integrated intensities of the SOPRA and Spex Raman lines. All integrated intensities presented here from the SOPRA spectra have been normalized to the Spex results.

Representative experimental spectra for the temperature dependence of the one-magnon scattering from the lower energy branch are shown in Fig. 2. In X(ZX)Y polarization, or equivalently X(ZY)Z polarization, the spectrum is dominated by the Stokes one-magnon peak whereas in X(YZ)Y polarization the anti-Stokes peak appears as the dominant feature. Stronger or weaker one-magnon scattering is also seen in X(YY)Z and X(YX)Z polarizations but in these cases the peak has similar Stokes and anti-Stokes intensities. No one-magnon scattering was observed in X(ZZ)Y and Z(XX)Y polarizations. Spectra were also recorded in Z(XZ)Y and Z(YZ)Y polarizations, and the results obtained were similar to those in X(YZ)Y polarization.

The temperature and polarization dependence of the one-magnon scattering from the upper branch is given in Fig. 3. Here, spectra in all polarizations are qualitatively similar in that the Stokes peak dominates at low temperatures while the anti-Stokes feature becomes more evident at higher temperatures owing to the greater number of thermally populated magnon states. However, as can be seen by comparing the spectra in X(YZ)Y and X(ZX)Y polarizations, the intensity of the one-magnon Raman peak shows quantitative differences between the various polarizations. The higher energy branch was also investigated in some polarizations with the SOPRA spectrometer to provide complementary information to the spectra obtained with the Spex spectrometer. The results obtained are shown in Fig. 4. The spectra are reassuringly quite similar to those shown in Fig. 2 with one exception. The much higher resolution of the SOPRA spectrometer reveals that the upper branch one-magnon peak is quite sharp and is notably resolution limited in width at 10.0 K.

Representative fits to the one-magnon Raman spectra are shown in Fig. 5. Generally, fits with PEAKFIT to the upper

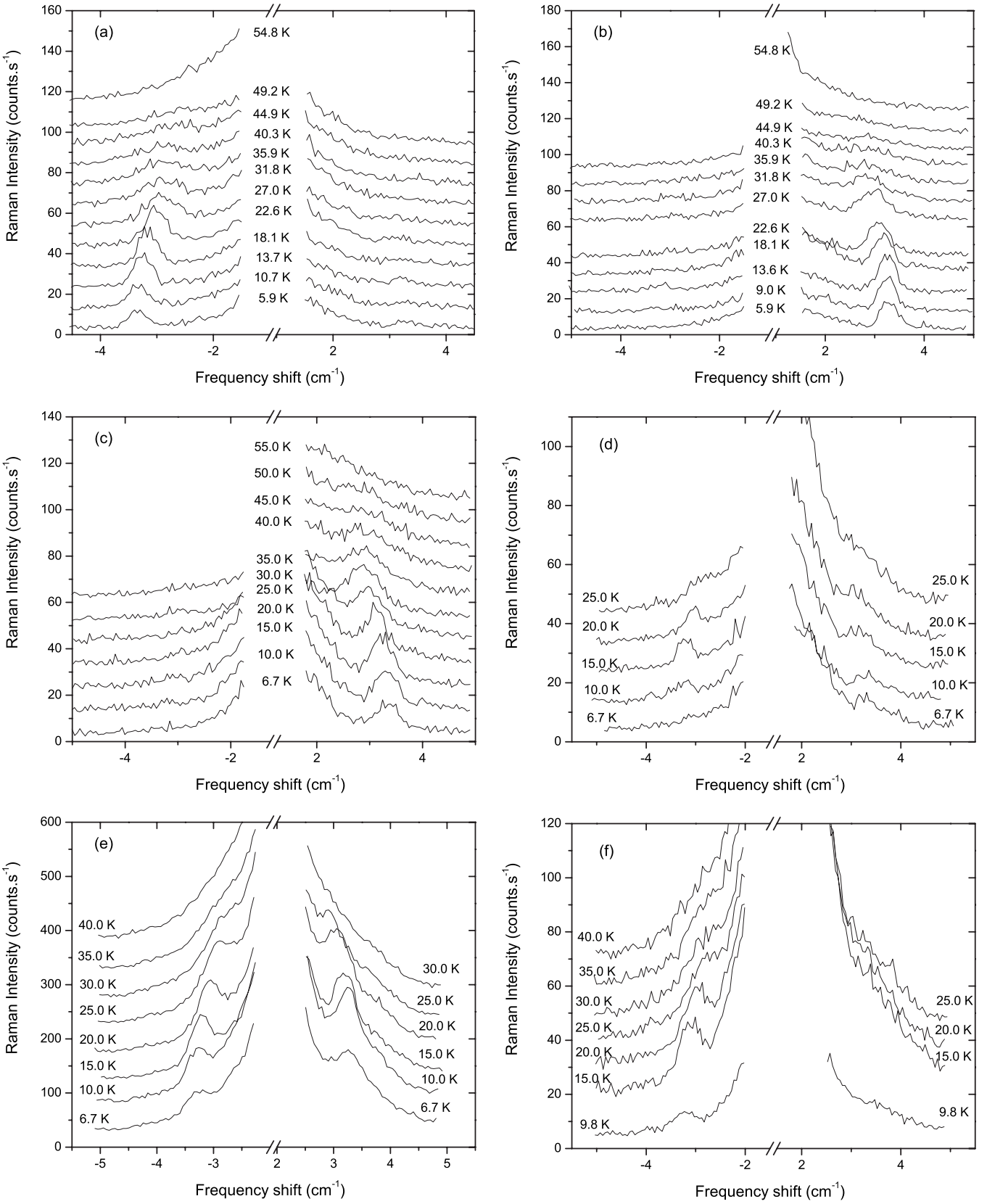

FIG. 2. Temperature dependence of the Stokes and anti-Stokes one-magnon lower branch Raman spectrum of NiF_2 in (a) X(YZ)Y, (b) X(ZX)Y, (c) X(ZY)Z, (d) X(YX)Z, (e) X(YY)Z, and (f) Z(XZ)Y polarizations, as recorded with the SOPRA spectrometer. The spectra at different temperatures have been offset vertically for clarity.

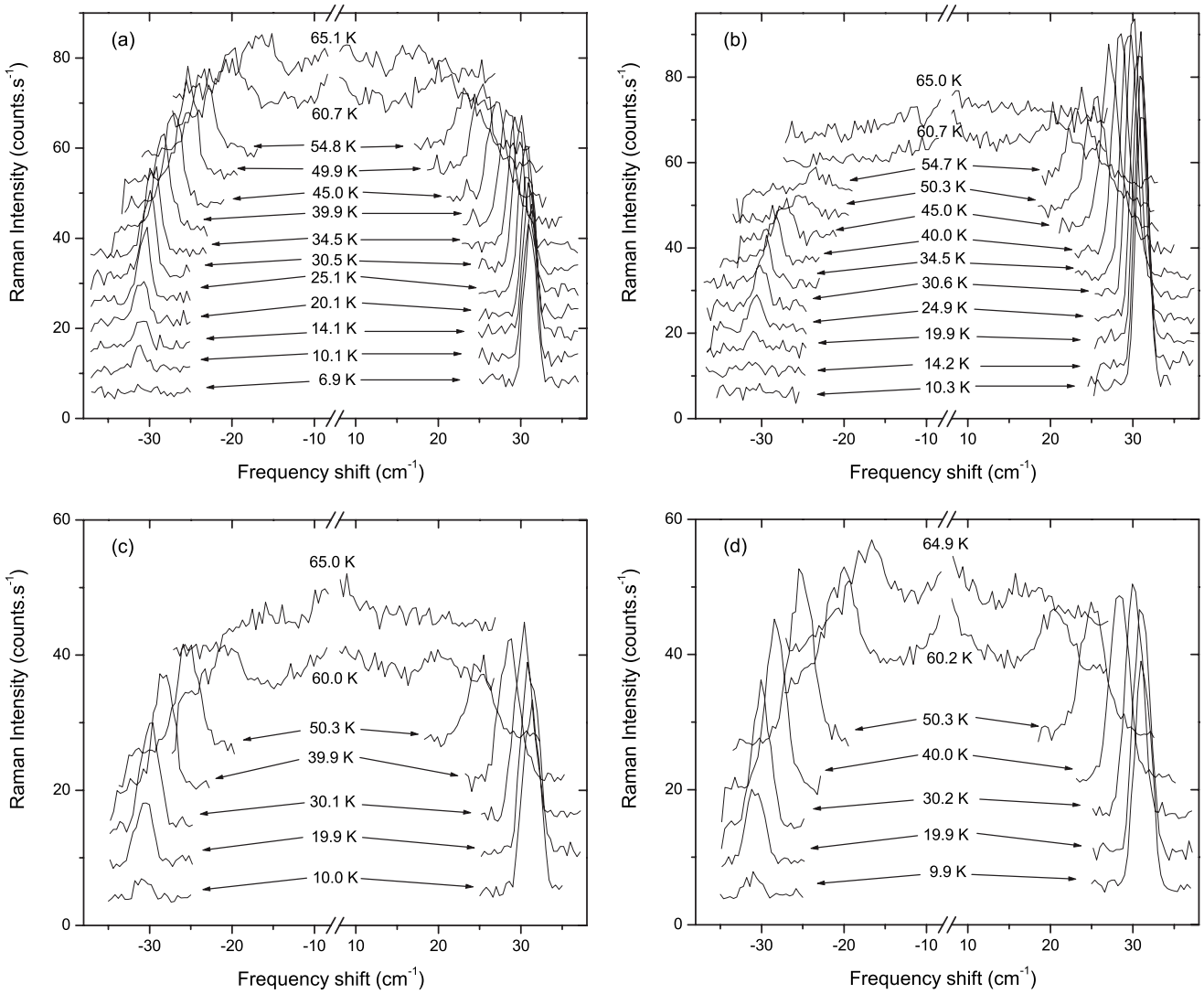

FIG. 3. Temperature dependence of the Stokes and anti-Stokes one-magnon upper branch Raman spectrum of NiF_2 in (a) X(YZ)Y, (b) X(ZX)Y, (c) Z(XZ)Y, and (d) Z(YZ)Y polarizations, as recorded with the Spex spectrometer. The spectra have been offset for clarity.

branch magnon could be readily obtained with a linear or flat background while those with PEAKFIT for the lower branch magnon required a nonlinear (exponential) rising background to lower frequency arising from the stray light within the spectrometer at the laser frequency. In the case of the fits with SP2, because of limitations in the fitting procedure, the rising background was fitted with a constant background combined with a Lorentzian centered at 0 cm^{-1}. Peak parameters of frequency, width, and integrated intensity obtained from the spectra through curve fitting are shown for the anti-Stokes and Stokes lower branch magnons in Figs. 6 and 7, respectively, and for the upper branch magnons in Figs. 8 and 9. The error bars given in these and later figures are the standard errors from the fits. In the case of the lower branch magnon, the two different computer analytical curve-fitting approaches, as mentioned above, were used by two different operators to fit the spectra and thus in Figs. 6 and 7 another set of data points is provided. The results of the second method have been plotted without error bars. The differences between the two sets of fitted results are another indicator of the experimental errors involved in the analysis of the lower branch magnon spectra, which is made more complicated by the rising background and weak magnon peak at higher temperatures.

For some polarizations the lower branch anti-Stokes magnon data are less certain than the corresponding Stokes data and vice versa for other polarizations but there is good agreement between the two sets of data for the temperature dependences of the peak frequency and linewidth. The fitted peak frequency of 3.31 ± 0.03 cm^{-1} at 5.9 K in X(ZX)Y and X(YZ)Y polarizations is in good agreement with the antiferromagnetic resonance (AFMR) value[4] of 3.33 ± 0.05^{-1}. The measured linewidth at 5.9 K is 0.40 ± 0.03 cm^{-1}, which allowing for the resolution of 0.42 cm^{-1} gives a natural linewidth of less than 0.01 cm^{-1}. The linewidth scarcely increases with temperature for temperatures up to 20 K, probably because it is still small compared to the resolution and then increases to about 2 cm^{-1} at 55 K. Meanwhile, the magnon peak frequency slowly decreases to about 2.5 cm^{-1} at 55 K and thus the lower branch magnon remains underdamped to quite high temperatures relative to T_N. Interestingly, there is a pronounced kink at 30–32 K in the tempera-

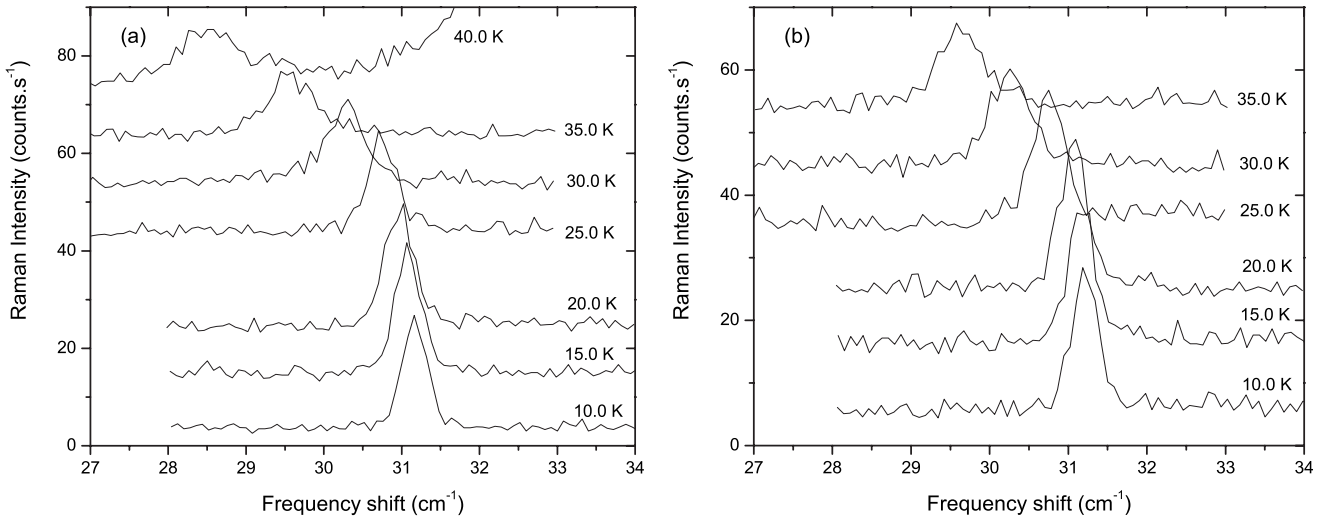

FIG. 4. Temperature dependence of the Stokes one-magnon upper branch Raman spectrum of NiF_2 in (a) Y(ZX)Z and (b) Y(ZY)Z polarizations, as recorded with the SOPRA spectrometer. The spectra have been offset for clarity.

ture dependence of the one-magnon frequency, which could be indicative of spin realignment.

Although the upper branch anti-Stokes magnon data are less certain than the corresponding Stokes data, because the anti-Stokes peak is weaker overall, there is good agreement between the two sets of data for the temperature dependences of the peak frequency and linewidth. At 9.0 K the peak frequency measured in Y(ZX)Z polarization at higher resolution on the SOPRA spectrometer is 31.13 ± 0.05 cm^{-1}, which compares well with low-temperature literature values of 31.14 ± 0.1 cm^{-1} from AFMR (Ref. 4) and ~ 31 cm^{-1} from Raman spectroscopy.[3,13–15] Like the lower branch magnon, the upper branch magnon scarcely shifts in frequency for temperatures up to 20 K but thereafter decreases steadily to about 17 cm^{-1} at 65 K. The lower branch magnon linewidth at 9.0 K is 0.43 ± 0.01 cm^{-1}, which allowing for the resolution of 0.42 cm^{-1} gives a natural linewidth of about 0.01 cm^{-1}. For comparison, a previous study of the linewidth by Rezende and da Silva[15] indicated a higher linewidth of 0.2 cm^{-1} at 6 K. The linewidth increases fairly slowly with temperature and is only about 4 cm^{-1} at 65 K and thus not only the lower branch magnon but also the upper branch magnon remains underdamped to quite high temperatures relative to T_N. A comparison of results obtained with the two spectrometer systems for the upper branch magnon is given in Figs. 8 and 9. Apart from the offset in the magnon linewidth owing to the two different spectral resolutions employed, there is very good agreement between the results obtained with the two systems.

III. THEORETICAL ANALYSIS

We first transform the spin operators to a new coordinate system such that the new z axis for each sublattice spin is in the direction of the (as yet unknown) equilibrium spin alignment. There will be a different transformation for each sublattice. For the i sublattice the transformation can be considered in two stages. The first stage is a cyclic permutation of the labels $(x,y,z) \rightarrow (z',x',y')$ while the second involves a rotation of $3\pi/4 - \theta$ about the y' axis, where θ denotes the canting angle. The overall transformation for sites on the i sublattice may then be written as

$$\begin{pmatrix} S_i^x \\ S_i^y \\ S_i^z \end{pmatrix} = \begin{pmatrix} -s_1 & 0 & -c_1 \\ -c_1 & 0 & s_1 \\ 0 & 1 & 0 \end{pmatrix} \begin{pmatrix} S_i^{x''} \\ S_i^{y''} \\ S_i^{z''} \end{pmatrix}, \tag{2}$$

where we denote $s_1 = \sin(\pi/4 + \theta)$ and $c_1 = \cos(\pi/4 + \theta)$. The overall transformation for j-sublattice sites is

$$\begin{pmatrix} S_j^x \\ S_j^y \\ S_j^z \end{pmatrix} = \begin{pmatrix} -c_1 & 0 & s_1 \\ -s_1 & 0 & -c_1 \\ 0 & -1 & 0 \end{pmatrix} \begin{pmatrix} S_j^{x''} \\ S_j^{y''} \\ S_j^{z''} \end{pmatrix}. \tag{3}$$

Using Eqs. (2) and (3) along with trigonometric identities, the NiF_2 Hamiltonian in Eq. (1) can now be expressed in terms of the new local coordinate system as (apart from a constant term)

$$\begin{aligned} H = \sum_{i,j} J_{i,j} \Big\{ & -\cos(2\theta) S_i^{z''} S_j^{z''} - \frac{1}{2}\sin^2\theta (S_i^+ S_j^- + S_i^- S_j^+) \\ & + \frac{1}{2}\cos^2\theta (S_i^+ S_j^+ + S_i^- S_j^-) - \frac{1}{2}\sin(2\theta)[(S_i^+ + S_i^-) S_j^{z''} + S_i^{z''}(S_j^+ \\ & + S_j^-)] \Big\} + \frac{1}{2}\sum_{i,i'} J'_{i,i'} \boldsymbol{S}_i \cdot \boldsymbol{S}_{i'} + \frac{1}{2}\sum_{j,j'} J'_{j,j'} \boldsymbol{S}_j \cdot \boldsymbol{S}_{j'} \\ & - P_1 [\sum_i (S_i^{z''})^2 + \sum_j (S_j^{z''})^2] - P_2 \{\sum_i [(S_i^+)^2 + (S_i^-)^2] \\ & + \sum_j [(S_j^+)^2 + (S_j^-)^2]\} - P_3 \{\sum_i [(S_i^+ S_i^{z''} + S_i^{z''} S_i^+) + (S_i^- S_i^{z''} \\ & + S_i^{z''} S_i^-)] + \sum_j [(S_j^+ S_j^{z''} + S_j^{z''} S_j^+) + (S_j^- S_j^{z''} + S_j^{z''} S_j^-)]\}. \end{aligned} \tag{4}$$

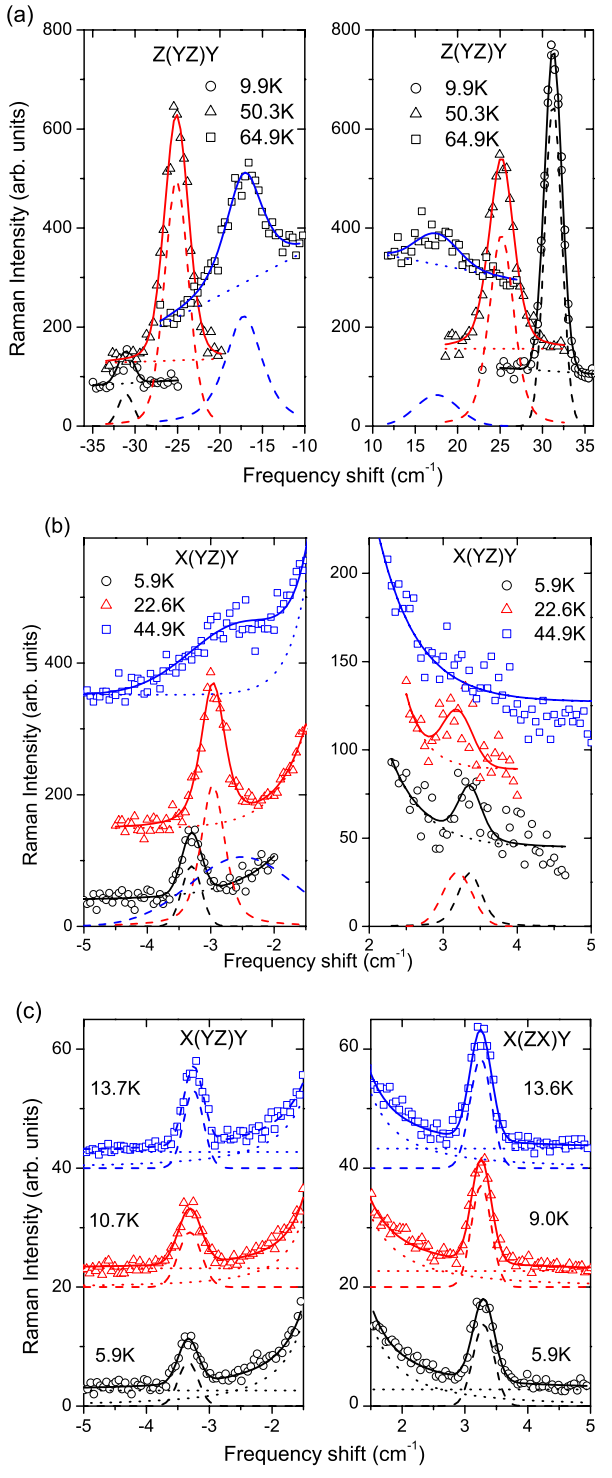

FIG. 5. (Color online) Representative fits obtained using the PEAKFIT software to the Stokes and anti-Stokes one-magnon Raman spectra at different temperatures for (a) the upper branch in Z(YZ)Y polarization and (b) the lower branch in X(YZ)Y polarization. (c) Representative fits to the Stokes and anti-Stokes spectra for the lower branch obtained with the SP2 software. The measured spectra are denoted by the open points while the fit is indicated by the solid line through the points. The dashed line indicates the fitted peak(s) and the dotted line is the background contribution in the fit. Note that for the Stokes scattering in X(YZ)Y polarization at 44.9 K there is no discernible magnon peak.

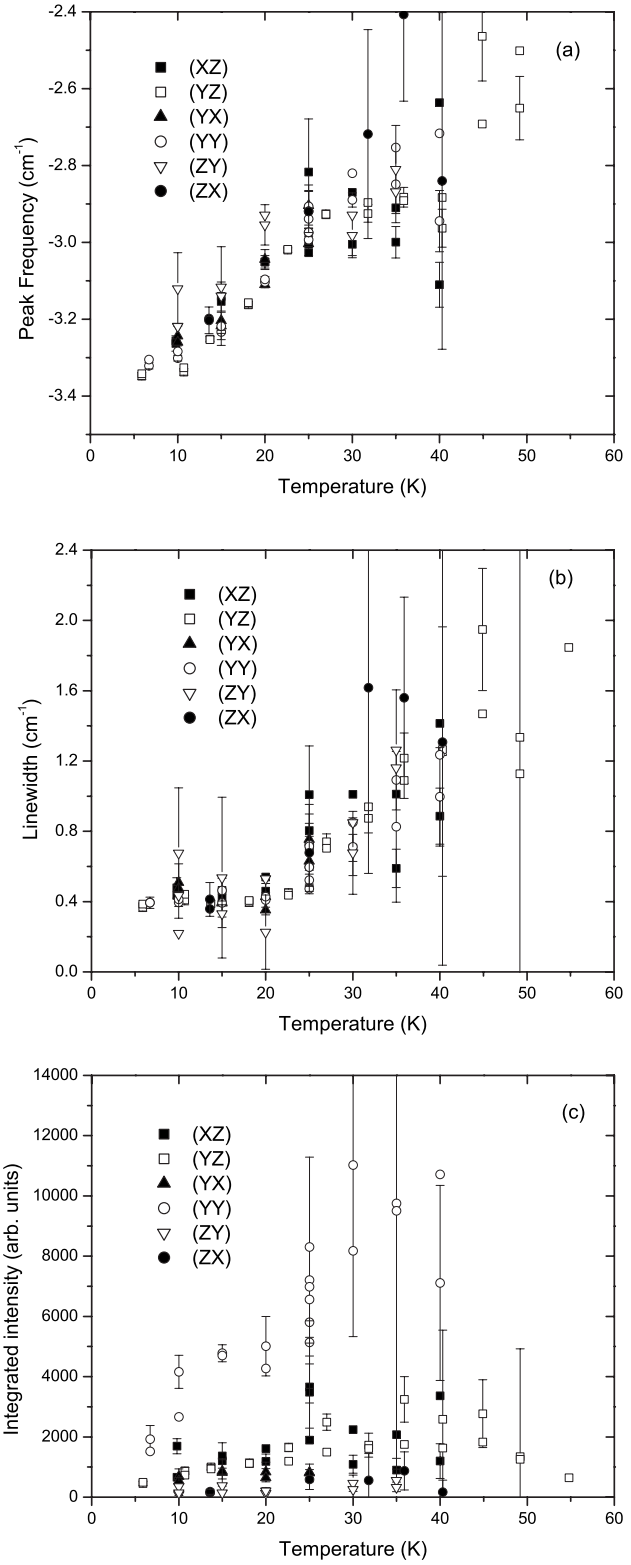

FIG. 6. Temperature dependence of the lower branch anti-Stokes one-magnon (a) peak frequency, (b) linewidth, and (c) integrated intensity in NiF_2 for various polarizations.

Here $S_i^{\pm}$ and $S_j^{\pm}$ are the raising and lowering operators defined with respect to the new axes and

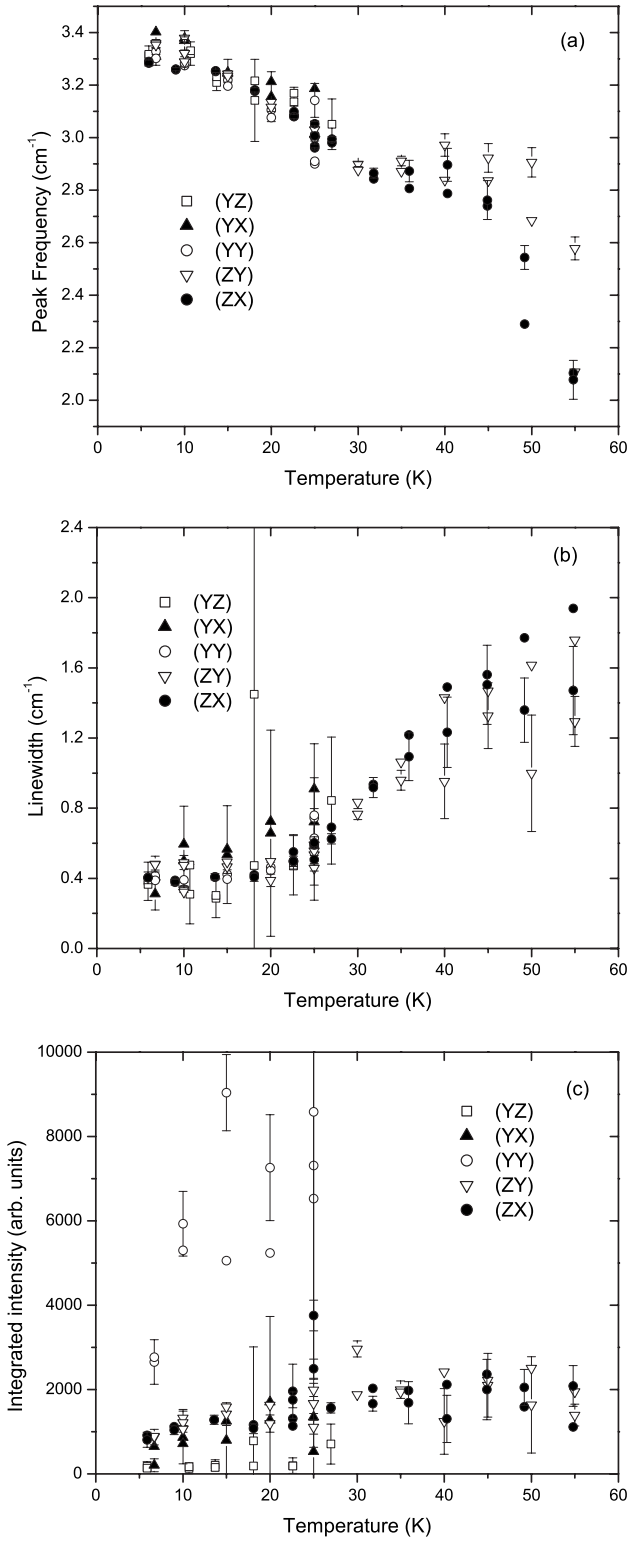

FIG. 7. Temperature dependence of the lower branch Stokes one-magnon (a) peak frequency, (b) linewidth, and (c) integrated intensity in NiF_2 for various polarizations.

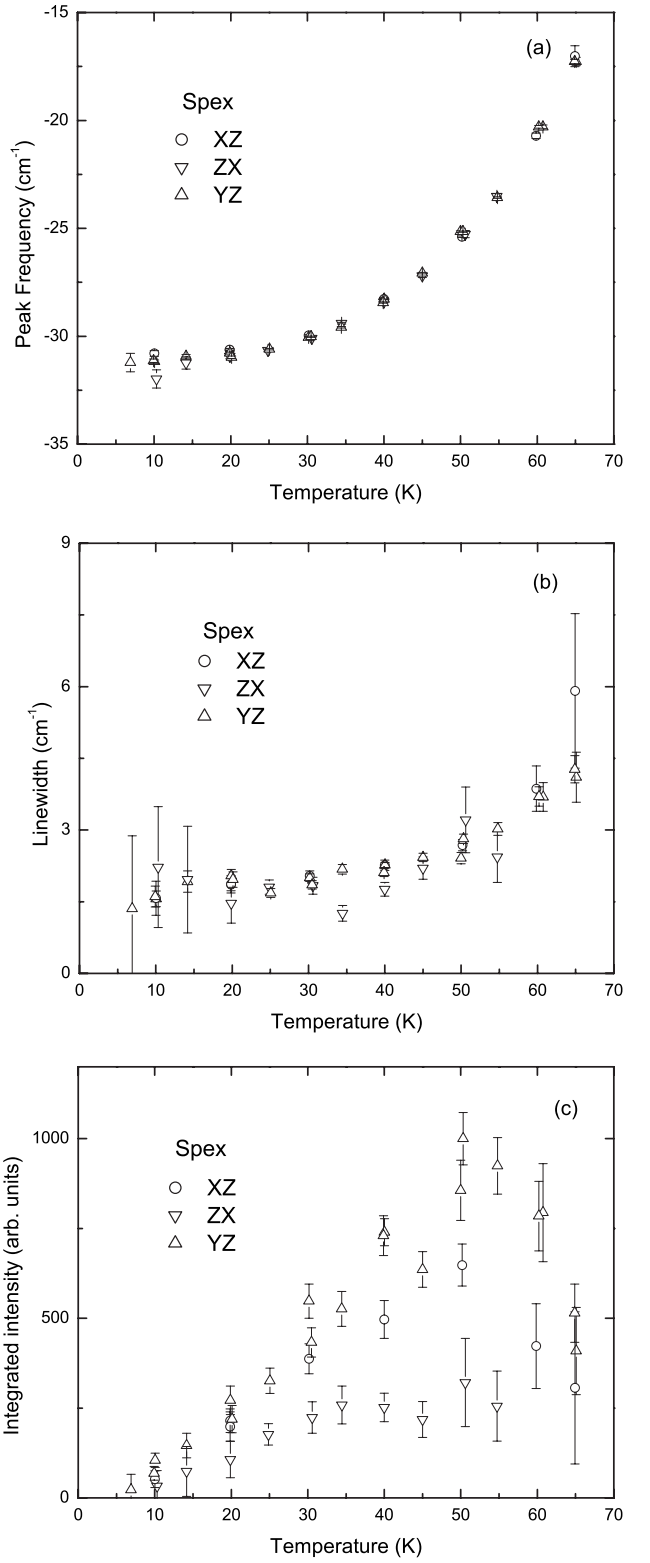

FIG. 8. Temperature dependence of the upper branch anti-Stokes one-magnon (a) peak frequency, (b) linewidth, and (c) integrated intensity in NiF_2 for various polarizations.

$$P_1 = \frac{1}{2}[D + 3F\sin(2\theta)],$$

$$P_2 = \frac{1}{4}[D - F\sin(2\theta)],$$

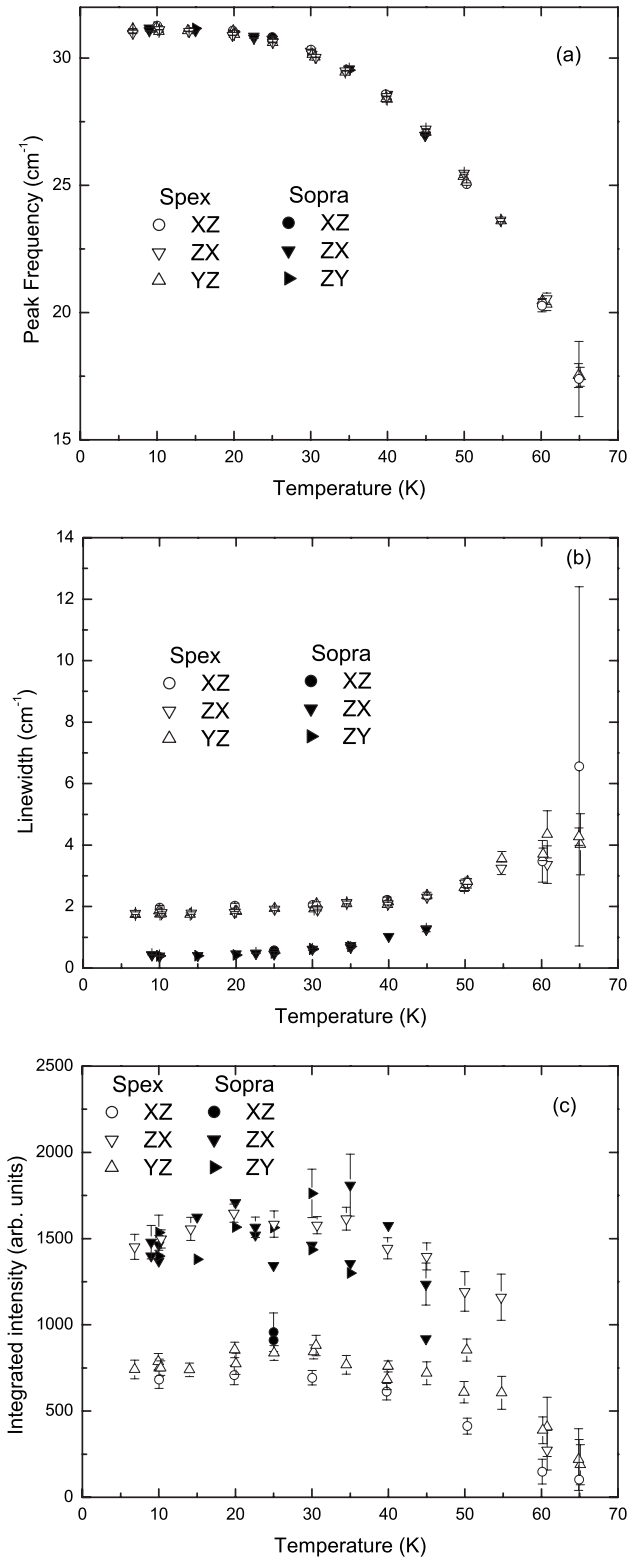

FIG. 9. Temperature dependence of the upper branch Stokes one-magnon (a) peak frequency, (b) linewidth, and (c) integrated intensity in NiF_2 for various polarizations.

$$P_3 = -\frac{1}{2}F\cos(2\theta). \tag{5}$$

Equations (4) and (5) are analogous to those obtained by Awang and Cottam[7] in studying one-magnon light scattering in the spin-flop region of antiferromagnets. The important difference in the present study is that the canting of the spins is a result of the intrinsic anisotropy of the system whereas in the spin-flop phase the canting is due to an applied magnetic field.

A. Canting angle

So far θ is undetermined. By analogy with Ref. 7 we consider making a decoupling approximation for the terms in the Hamiltonian H that are linear in the transverse spin component, i.e., the exchange terms proportional to $\sin(2\theta)$ and the anisotropy terms proportional to P_3. Taking the case of sites on the i sublattice, the usual random-phase approximation decoupling approximation applied to the exchange term yields

$$(S_i^+ + S_i^-)S_j^{z''} \rightarrow (S_i^+ + S_i^-)\langle S_j^{z''}\rangle \rightarrow (S_i^+ + S_i^-)S \quad \text{for} \quad T \ll T_N. \tag{6}$$

For the anisotropy term we use the Anderson-Callen[8] decoupling approximation

$$(S_i^+ S_i^{z''} + S_i^{z''} S_i^+) + (S_i^- S_i^{z''} + S_i^{z''} S_i^-) \rightarrow 2\langle S_i^{z''}\rangle p(T)(S_i^+ + S_i^-)$$
$$\rightarrow 2Sp(0)(S_i^+ + S_i^-) \quad \text{for} \quad T \ll T_N, \tag{7}$$

where $p(T)$ is a temperature-dependent decoupling parameter.[7] The decoupling in Eq. (6) neglects any correlation between the longitudinal and transverse spin components on different sites. The terms appearing on the left-hand side of Eq. (7) involve the product of operators at the *same* site and so this decoupling is an approximation concerning the spin statistics at the particular site.

The stability condition requires the overall coefficient of the transverse spin components $(S^+ + S^-)$ to vanish (since, by definition, the new axes are in the direction of local spin alignment). Substituting for P_3 and rearranging gives

$$\tan(2\theta) = \frac{2p(T)F}{8J_2}. \tag{8}$$

In NiF_2 $F \ll 8J_2$ and thus the canting angle may be written as $\theta \approx p(T)F/8J_2$.

B. Spin-dependent Green's functions at low temperatures

We begin by forming the equation of motion for Green's functions of the type $\langle\langle S_l^+; Y\rangle\rangle_E$, where l represents a particular site on the i sublattice and Y will be chosen later. By analogy with work on spin-flop antiferromagnets,[7] the equation may be written in a position representation as

$$E\langle\langle S_l^+; Y\rangle\rangle_E = \frac{1}{2\pi}\langle [S_l^+, Y]\rangle + \sum_j J_{l,j}\{\cos(2\theta)\langle\langle S_l^+ S_j^{z''}; Y\rangle\rangle_E$$
$$- \sin^2(\theta)\langle\langle S_l^{z''} S_j^+; Y\rangle\rangle_E + \cos^2(\theta)\langle\langle S_l^{z''} S_j^-; Y\rangle\rangle_E\}$$
$$+ \sum_{i'} J'_{l,i'}\{\langle\langle S_l^{z''} S_{i'}^+ - S_l^+ S_{i'}^{z''}; Y\rangle\rangle_E\} + P_1\langle\langle S_l^+ S_l^{z''}$$
$$+ S_l^{z''} S_l^+; Y\rangle\rangle_E - 2P_2\langle\langle S_l^- S_l^{z''} + S_l^{z''} S_l^-; Y\rangle\rangle_E. \tag{9}$$

Next we linearize the Green's functions appearing on the right-hand side (RHS) of Eq. (9) using Eqs. (6) and (7) to decouple products of spin operators. Then the equations of motion of the new Green's functions are formed and the resulting closed set of equations is transformed to a wave-vector representation.

For simplicity we first consider the low-temperature case of $T \ll T_N$ so that thermal averages like $\langle S_l^{z''} \rangle$ may be replaced by the spin S. The final result may be written compactly in a matrix form as

$$\begin{pmatrix} E-\Omega & \alpha & \delta & -\gamma \\ -\alpha & E+\Omega & \gamma & -\delta \\ \delta & -\gamma & E-\Omega & \alpha \\ \gamma & -\delta & -\alpha & E+\Omega \end{pmatrix} \begin{pmatrix} G_{1\mathbf{k}} \\ G_{2\mathbf{k}} \\ G_{3\mathbf{k}} \\ G_{4\mathbf{k}} \end{pmatrix} = \begin{pmatrix} b_1^+ \\ b_1^- \\ b_2^+ \\ b_2^- \end{pmatrix}, \tag{10}$$

where $G_{1\mathbf{k}}$, $G_{2\mathbf{k}}$, $G_{3\mathbf{k}}$, and $G_{4\mathbf{k}}$ are the Fourier components of $\langle\langle S_l^+; Y\rangle\rangle_E$, $\langle\langle S_l^-; Y\rangle\rangle_E$, $\langle\langle S_m^+; Y\rangle\rangle_E$, and $\langle\langle S_m^-; Y\rangle\rangle_E$, respectively, at wave vector $\mathbf{k}$. Here the label m represents a site on the j sublattice. The matrix parameters are defined by

$$\Omega = S\cos(2\theta)J_2(0) + 2Sp(0)P_1 + S[J_1(0) + J_3(0) - J_1(\mathbf{k}) - J_3(\mathbf{k})],$$

$$\alpha = 4Sp(0)P_2,$$

$$\delta = S\sin^2\theta J_2(\mathbf{k}),$$

$$\gamma = S\cos^2\theta J_2(\mathbf{k}) \tag{11}$$

and the Fourier components of the exchange terms are

$$J_1(\mathbf{k}) = 2J_1\cos(k_z c),$$

$$J_2(\mathbf{k}) = 8J_2\cos(k_x a/2)\cos(k_y a/2)\cos(k_z c/2),$$

$$J_3(\mathbf{k}) = 2J_3[\cos(k_x a) + \cos(k_y a)]. \tag{12}$$

The inhomogeneous terms appearing on the RHS of Eq. (10) involve thermal averages defined as $b_1^\pm = (1/2\pi)\langle[S_l^\pm, Y]\rangle$ and $b_2^\pm = (1/2\pi)\langle[S_m^\pm, Y]\rangle$. Writing Eq. (10) as $\tilde{A}\mathbf{G}_\mathbf{k} = \boldsymbol{b}$, the Green's functions $\boldsymbol{G}_\mathbf{k}$ may be obtained by inverting the matrix $\tilde{A}$. The magnon energies correspond to the poles of the Green's functions and are obtained from the determinant condition $\det\tilde{A} = 0$. To achieve this, as well as the matrix inversion, $\tilde{A}$ can first be expressed in partitioned form as

$$\tilde{A} = \begin{pmatrix} M_1 & M_2 \\ M_2 & M_1 \end{pmatrix}, \tag{13}$$

where M_1 and M_2 are 2×2 block matrices. Introducing the transformation matrix

$$\tilde{N} = \frac{1}{2}\begin{pmatrix} C & C \\ C & -C \end{pmatrix} \quad \text{where} \quad C = \begin{pmatrix} 1 & 1 \\ 1 & -1 \end{pmatrix}, \tag{14}$$

we can write $\tilde{A} = \tilde{N}\tilde{D}\tilde{N}$. Here $\tilde{D}$ is the block-diagonal matrix defined as

$$\tilde{D} = \begin{pmatrix} D_1 & 0 \\ 0 & D_2 \end{pmatrix}. \tag{15}$$

The magnon energies are now readily obtained from the determinant conditions $\det D_1 = 0$ and $\det D_2 = 0$, and the results are

$$E_1(\mathbf{k}) = \sqrt{(\Omega-\delta)^2 - (\gamma-\alpha)^2},$$

$$E_2(\mathbf{k}) = \sqrt{(\Omega+\delta)^2 - (\gamma+\alpha)^2}, \tag{16}$$

so there are two branches as anticipated. Since one-magnon light scattering involves only excitations near the zone center we set $\mathbf{k} \approx 0$. The approximate zone-center magnon energies are obtained by expanding the terms in the square root up to second order in the small angle θ and may eventually written as

$$E_1(0) = \sqrt{4p(0)DJ_2(0) + 4S^2p(0)^2F^2},$$

$$E_2(0) = 4Sp(0)F. \tag{17}$$

Using properties of the transformation matrix the solution to the inhomogeneous Eq. (10) may be written as

$$\boldsymbol{G}_\mathbf{k} = \tilde{A}^{-1}\boldsymbol{b} = (\tilde{N}\tilde{D}^{-1}\tilde{N})\boldsymbol{b} = \tilde{N}\begin{pmatrix} D_1^{-1} & 0 \\ 0 & D_2^{-1} \end{pmatrix}\tilde{N}\boldsymbol{b}. \tag{18}$$

If we now choose the operator Y to be equal to $S_l^\pm$ and $S_m^\pm$ in turn, we can obtain 16 Green's functions. These are required to evaluate the correlation functions that appear later in the one-magnon scattering cross section. Using the properties of the matrix $\tilde{A}$, along with the general property that $\langle\langle X; Y\rangle\rangle_E = \langle\langle Y; X\rangle\rangle_{-E}$, all of the required Green's functions can be obtained from the following set, taking accounting of the different sublattice labels for the spin operators:

$$\langle\langle S_l^+; S_i^+\rangle\rangle_E = \langle\langle S_l^-; S_i^-\rangle\rangle_E = \frac{R}{N}\sum_\mathbf{k}\exp(i\mathbf{k}\cdot\mathbf{r}_{li})\left\{\frac{\alpha-\gamma}{E^2 - E_1(\mathbf{k})^2} + \frac{\gamma+\alpha}{E^2 - E_2(\mathbf{k})^2}\right\},$$

$$\langle\langle S_l^+; S_i^-\rangle\rangle_E = \frac{R}{N}\sum_\mathbf{k}\exp(i\mathbf{k}\cdot\mathbf{r}_{li})\left\{\frac{E+\Omega-\delta}{E^2 - E_1(\mathbf{k})^2} + \frac{E+\Omega+\delta}{E^2 - E_2(\mathbf{k})^2}\right\},$$

$$\langle S_l^+; S_j^+\rangle_E = \langle\langle S_l^-; S_j^-\rangle\rangle_E = \frac{R}{N}\sum_\mathbf{k}\exp(i\mathbf{k}\cdot\mathbf{r}_{lj})\left\{\frac{\alpha-\gamma}{E^2 - E_1(\mathbf{k})^2} - \frac{\gamma+\alpha}{E^2 - E_2(\mathbf{k})^2}\right\},$$

$$\langle\langle S_l^+; S_j^-\rangle\rangle_E = \frac{R}{N}\sum_\mathbf{k}\exp(i\mathbf{k}\cdot\mathbf{r}_{lj})\left\{\frac{E+\Omega-\delta}{E^2 - E_1(\mathbf{k})^2} - \frac{E+\Omega+\delta}{E^2 - E_2(\mathbf{k})^2}\right\}. \tag{19}$$

Here we have defined $\mathbf{r}_{ij} = \mathbf{r}_i - \mathbf{r}_j$ and $R = \langle S^z\rangle/2\pi \to S/2\pi$ at $T \ll T_N$. Also the decoupling parameter p in the low-temperature limit becomes $p(0) = (1 - 1/2S)$, consistent with spin-wave theory.[8]

A low-temperature theory may alternatively be carried out using an expansion in terms of boson operators, e.g., as was done by Hutchings *et al.*[3] for the excitation energies, leading to similar results. However, there are difficulties in achieving self-consistency for the decoupling approximations.[3] Thus the spin operator method used here is preferable and also it can be applied at higher temperatures.

C. Extension to higher temperatures

To extend the previous results to higher temperatures we again decouple the product of operators at the *same* site using the scheme proposed by Anderson and Callen[8] in their investigations of phase transitions in uniaxial antiferromagnets. However, the temperature-dependent decoupling parameter in Eq. (7) has the generalized form

$$p(T) = 1 - (1/2S^2)[S(S+1) - \langle (S^{z''})^2 \rangle], \tag{20}$$

where $\langle (S^{z''})^2 \rangle$ represents a static thermal average. Other decoupling approximations have been proposed (see Ref. 16) but for small spin values such as $S=1$ all these approximations give essentially identical results. The above decoupling term satisfies the condition that $p=0$ for $S=1/2$ while for a general spin value it reduces to the low-temperature value quoted earlier.

Generalizing the approach used in the previous section, we now find that the zone-center excitation energies for NiF_2 may be written as

$$E_1(0) = \langle S^{z''} \rangle (2\langle (S^{z''})^2 \rangle DJ_2(0) + \langle (S^{z''})^2 \rangle^2 F^2)^{1/2},$$

$$E_2(0) = 2\langle S^{z''} \rangle \langle (S^{z''})^2 \rangle F. \tag{21}$$

The static thermal averages $\langle S^{z''} \rangle$ and $\langle (S^{z''})^2 \rangle$ may next be approximated using a modified mean-field theory similar to that used in Ref. 7 for the spin-flop phase of an antiferromagnet. The method involves writing down an effective Hamiltonian $\mathcal{H}_{eff}$ for the canted antiferromagnet using a mean-field theory to simplify the exchange terms in Eq. (4) while treating the single-ion anisotropy terms exactly. For the i sublattice the effective Hamiltonian is

$$\mathcal{H}_{eff} = -\sum_i \left\{ h_1 S_i^{z''} + \frac{1}{2} h_2 (S_i^+ + S_i^-) + P_1 (S_i^{z''})^2 + P_2 [(S_i^+)^2 + (S_i^-)^2] + P_3 [(S_i^+ S_i^{z''} + S_i^{z''} S_i^+) + (S_i^- S_i^{z''} + S_i^{z''} S_i^-)] \right\}, \tag{22}$$

where

$$h_1 = \langle S^{z''} \rangle \{ J_2(0)\cos(2\theta) + [J_1(0) + J_3(0)], \}$$

$$h_2 = \langle S^{z''} \rangle J_2(0)\sin(2\theta). \tag{23}$$

Using the standard 3×3 matrix representation of the spin $S=1$ operators the effective Hamiltonian $\mathcal{H}_{eff}$ may be written as

$$\mathcal{H}_{eff} = \begin{pmatrix} -(h_1 + P_1) & (-1/\sqrt{2})(h_2 + 2P_3) & -2P_2 \\ (-1/\sqrt{2})(h_2 + 2P_3) & 0 & (-1/\sqrt{2})(h_2 - 2P_3) \\ -2P_2 & (-1/\sqrt{2})(h_2 - 2P_3) & (h_1 - P_1) \end{pmatrix}. \tag{24}$$

If the linear terms in the transverse spin components are decoupled as before, all of the leading off-diagonal elements of $\mathcal{H}_{eff}$ vanish and the canting angle is a temperature-dependent quantity obtained from the stability condition $h_2 = -4\langle S_i^{z''} \rangle p(T) P_3$.

An alternative procedure is as follows. The canting angle may be deduced from the condition that the thermal averages $\langle S_i^+ \rangle$ and $\langle S_j^+ \rangle$ must be zero because the transverse spin components for each sublattice are defined with respect to the local sublattice alignment. The mean-field Hamiltonian (24) may be diagonalized by the transformation $\tilde{\mathcal{H}}_{eff} = \mathbf{U}^{-1} \mathcal{H}_{eff} \mathbf{U}$. Although it is possible to solve analytically for the matrix $\mathbf{U}$, the expressions are generally very complicated and make the solution of the equilibrium condition intractable. Instead we shall proceed numerically, noting that the thermal average of any operator at site i can be written as

$$\langle X_i \rangle = \mathrm{Tr}[\tilde{X}_i \exp(-\beta \tilde{H}_{eff})]/\mathrm{Tr}[\exp(-\beta \tilde{H}_{eff})], \tag{25}$$

where $\tilde{X}_i = \mathbf{U}^{-1} X_i \mathbf{U}$ and $\beta = 1/k_B T$. Replacing the operator X_i with $S_i^{z''}$ and $(S_i^{z''})^2$ we can obtain expressions for $\langle S_i^{z''} \rangle$ and $\langle (S_i^{z''})^2 \rangle$. Analogous expressions apply for sites on the j sublattice. The canting angle and the static thermal averages are found by following the numerical procedure: (i) for a given value of θ, calculate the eigenvalues and the transformation matrix $\mathbf{U}$. (ii) Deduce the sublattice averages $\langle S_i^{z''} \rangle$, $\langle S_j^{z''} \rangle$, $\langle S_i^+ \rangle$, and $\langle S_j^+ \rangle$, as described. (iii) Repeat for different θ (with θ incrementing in small steps) to search for the value of θ corresponding to the equilibrium condition $\langle S_i^+ \rangle = \langle S_j^+ \rangle = 0$ and converge on the solution. (iv) Using this value of θ, evaluate the required thermal averages and hence the magnon energies. (v) Repeat for higher temperatures.

The small corrections introduced in the latter case from the leading off-diagonal terms in $\mathcal{H}_{eff}$ are found to have a perturbing effect on the eigenvalues and eigenvectors when applied to NiF_2. At all temperatures the canting angle obtained using the two approaches are very similar, as might be expected and thus we use the former approach for simplicity. The results are illustrated Fig. 10, including comparisons with experimental data. It is seen that the theoretical results

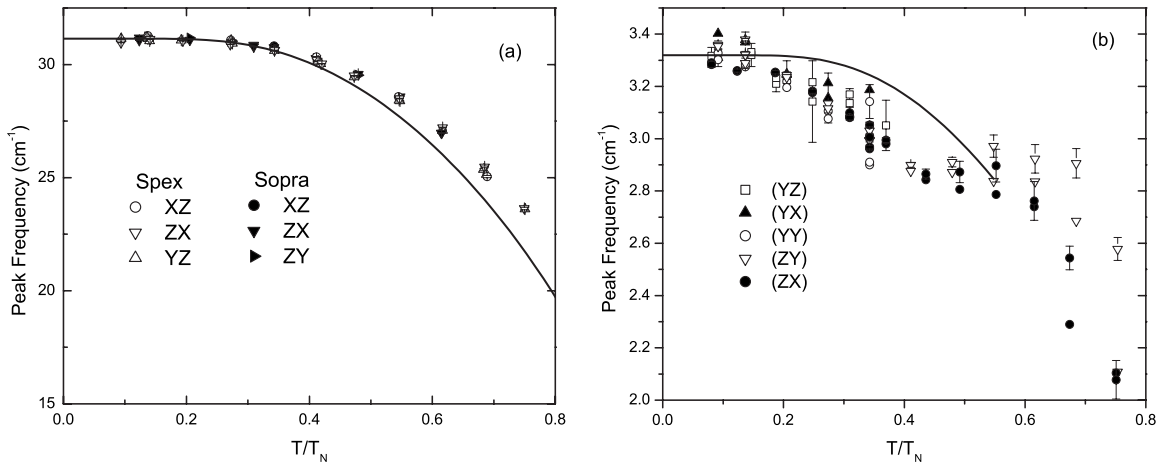

FIG. 10. Comparison of theory (solid lines) and experimental data for the upper (a) and lower (b) one-magnon energies versus reduced temperature. The theory lines are evaluated using the method outlined in Sec. III C.

for the upper branch are in good agreement with experiment up to $T/T_N \sim 0.4$, whereas for the lower branch the theory gives reasonable agreement up to $T/T_N \sim 0.2$.

The small jump by 0.2–0.3 cm^{-1} at around 31 K in the temperature dependence of the frequency of the lower branch magnon is not observed in the upper branch and thus it is likely due to a spin-reorientation effect in the crystal *a*-*b* plane. Based on this slight frequency change, the reorientation must be very small and would not involve a "major" spin realignment that would break the existing magnetic symmetry, as such a change would have been noted previously. The experimental data indicate that the spin reorientation in the *a*-*b* plane increases slightly the angle of spin deviation away from the *a* axis direction (see Fig. 1). Such a spontaneous spin reorientation with temperature change has been observed previously in orthoferrites[17] such as $ErFeO_3$ but has not been reported in NiF_2 or other rutile-structure antiferromagnets.[2] From Eq. (8) it is apparent that the lower branch magnon energy is proportional to F, which is proportional to the canting angle θ. Thus a 0.2–0.3 cm^{-1} shift in $E_2(0)$, which is approximately 2.9 cm^{-1} at 31 K, is a 7–10 % variation. The corresponding percentage variation in θ, assuming its value is somewhere around 0.4° or 0.5° at that temperature, leads to a change in θ of order 0.03°–0.045°. The angular change in the spin orientation is thus very small and could easily have been overlooked in the earlier neutron-scattering studies. Further such experimental investigations are now warranted.

IV. ONE-MAGNON SCATTERING CROSS SECTION

The one-magnon light-scattering cross section is evaluated following the general approach used in Refs. 9–11. Briefly, the spin-dependent susceptibility χ is expanded in terms of spin operators and includes the effects of linear K and quadratic G magneto-optical coefficients. These are known to play an important role in the one-magnon scattering in numerous magnetic systems (e.g., yttrium iron garnet and FeF_2) (Refs. 11 and 18) and so we allow for both terms here.

For sites on the i sublattice we write

$$\chi(\mathbf{r}_i) = \mathbf{V}_1 S_i^x + \mathbf{V}_2 S_i^y + \mathbf{V}_3 S_i^z + \mathbf{V}_4 (S_i^z S_i^x + S_i^x S_i^z) + \mathbf{V}_5 (S_i^z S_i^y + S_i^y S_i^z) + \mathbf{V}_6 (S_i^x S_i^y + S_i^y S_i^x). \tag{26}$$

Here the spin operators are defined with respect to the global coordinate system and the matrices in Eq. (26) are

$$\mathbf{V}_1 = \begin{pmatrix} 0 & 0 & 0 \\ 0 & 0 & iK_1 \\ 0 & -iK_1 & 0 \end{pmatrix}, \quad \mathbf{V}_2 = \begin{pmatrix} 0 & 0 & -iK_2 \\ 0 & 0 & 0 \\ iK_2 & 0 & 0 \end{pmatrix}, \quad \mathbf{V}_3 = \begin{pmatrix} 0 & iK_3 & 0 \\ -iK_3 & 0 & 0 \\ 0 & 0 & 0 \end{pmatrix},$$

$$\mathbf{V}_4 = \begin{pmatrix} 0 & 0 & G_1 \\ 0 & 0 & 0 \\ G_1 & 0 & 0 \end{pmatrix}, \quad \mathbf{V}_5 = \begin{pmatrix} 0 & 0 & 0 \\ 0 & 0 & G_2 \\ 0 & G_2 & 0 \end{pmatrix}, \quad \mathbf{V}_6 = \begin{pmatrix} 0 & G_3 & 0 \\ G_3 & 0 & 0 \\ 0 & 0 & 0 \end{pmatrix}. \tag{27}$$

By symmetry there may be three linear coefficients K_n (with $n=1,2,3$) and three quadratic coefficients G_n. For sites on the j sublattice the analogous result is

$$\chi(\mathbf{r}_j) = \mathbf{V}_1' S_j^x + \mathbf{V}_2' S_j^y + \mathbf{V}_3 S_j^z + \mathbf{V}_4' (S_j^z S_j^x + S_j^x S_j^z) + \mathbf{V}_5' (S_j^z S_j^y + S_j^y S_j^z) + \mathbf{V}_6 (S_j^x S_j^y + S_j^y S_j^x). \tag{28}$$

The matrices $\mathbf{V}_1'$ and $\mathbf{V}_2'$ are obtained from Eq. (27) by interchanging K_1 and K_2 while $\mathbf{V}_4'$ and $\mathbf{V}_5'$ are obtained by interchanging G_1 and G_2. The sites on different sublattices of NiF_2 do not have identical symmetries because of the fluorine ions, so it is not necessarily the case (as it would be for simple tetragonal antiferromagnets) that $K_1=K_2$ and $G_1=G_2$. Finally, if we assume that there is no appreciable optical absorption the susceptibility tensor is Hermitian and the magneto-optical coefficients are real quantities. The spin op-

erators in Eqs. (26) and (28) can be transformed to the local coordinate system using Eqs. (2) and (3).

Next, we define the total spin-dependent susceptibility χ by

$$\chi = \sum_i \chi(\mathbf{r}_i) + \sum_j \chi(\mathbf{r}_j). \tag{29}$$

The only matrix components required to describe one-magnon light scattering[11] may eventually be written as

$$\chi^{xy} = \frac{K_3}{2}\sum_{ij}[(S_i^+ - S_i^-) - (S_j^+ - S_j^-)] - \frac{G_3}{2}\sin(2\theta)\sum_{ij}[(B_i + C_i) - (B_j + C_j)],$$

$$\chi^{xz} = i\frac{K^+}{2}\sum_{ij}[c_1(S_i^+ + S_i^-) + s_1(S_j^+ + S_j^-)] + i\frac{K^-}{2}\sum_{ij}[-c_1(S_i^+ + S_i^-) + s_1(S_j^+ + S_j^-)] + i\frac{G^+}{2}\sum_{ij}[c_1(B_i - C_i) + s_1(B_j - C_j)] + i\frac{G^-}{2}\sum_{ij}[c_1(B_i - C_i) - s_1(B_j - C_j)],$$

$$\chi^{yz} = i\frac{K^+}{2}\sum_{ij}[-s_1(S_i^+ + S_i^-) - c_1(S_j^+ + S_j^-)] + i\frac{K^-}{2}\sum_{ij}[-s_1(S_i^+ + S_i^-) + c_1(S_j^+ + S_j^-)] - i\frac{G^+}{2}\sum_{ij}[s_1(B_i - C_i) + c_1(B_j - C_j)] - i\frac{G^-}{2}\sum_{ij}[-s_1(B_i - C_i) + c_1(B_j - C_j)], \tag{30}$$

where $s_1 = \sin(\theta + \pi/4)$ and $c_1 = \sin(\theta + \pi/4)$. Also we introduce the shorthand notations $B = (S^+S^z + S^zS^+)$, $C = (S^-S^z + S^zS^-)$, $K^\pm = (K_1 \pm K_2)/2$, and $G^\pm = (G_1 \pm G_2)/2$. For simplicity we shall henceforth restrict attention to the following polarization types: (i) (YZ) and (ZY), and (ii) (YX).

The one-magnon differential scattering cross section in the (YZ) polarization may be written as[2]

$$\left(\frac{d^2h}{d\Omega d\omega_S}\right)_{YZ} = \frac{\mathcal{F}}{\{1 - \exp(-\beta E)\}}\mathrm{Im}\langle\langle \chi^{YZ}; (\chi^{YZ})^* \rangle\rangle_{E+i\epsilon}, \tag{31}$$

where the factor $\mathcal{F}$ is independent of temperature and scattering geometry. The higher order Green's functions (in terms of products of spin operators) that appear in $\langle\langle \chi^{YZ}; (\chi^{YZ})^* \rangle\rangle$ can now be decoupled using the procedures outlined in Sec. III C. For example, we obtain

$$\langle\langle B_l; S_i^+ \rangle\rangle_E = 2\langle S_l^{z''} \rangle p(T) \langle\langle S_l^+; S_i^+ \rangle\rangle_E,$$

$$\langle\langle B_l; C_i \rangle\rangle_E = 4\langle S_i^{z''} \rangle \langle S_l^{z''} \rangle p^2(T) \langle\langle S_l^+; S_i^- \rangle\rangle_E, \tag{32}$$

along with similar expression for sites on the j sublattice. The relevant expressions for the Green's functions on the RHS of Eq. (32) have already been given in Eq. (19).

TABLE I. Polarization-dependent terms appearing in Eq. (34) where $\kappa^\pm = K^+ \pm K^-$ and $\mathcal{G}^\pm = G^+ \pm G^-$.

Polarization	$L_1^\pm$	$L_2^\pm$
YZ	$-s_1[\kappa^+ \pm 2\langle S^z\rangle p(T)\mathcal{G}^-]$	$-c_1[\kappa^- \pm 2\langle S^z\rangle p(T)\mathcal{G}^+]$
ZY	$s_1[\kappa^+ \mp 2\langle S^z\rangle p(T)\mathcal{G}^-]$	$c_1[\kappa^- \mp 2\langle S^z\rangle p(T)\mathcal{G}^+]$
XZ	$c_1[\kappa^- \pm 2\langle S^z\rangle p(T)\mathcal{G}^+]$	$s_1[\kappa^+ \pm 2\langle S^z\rangle p(T)\mathcal{G}^-]$
ZX	$-c_1[\kappa^- \mp 2\langle S^z\rangle p(T)\mathcal{G}^+]$	$-s_1[\kappa^+ \mp 2\langle S^z\rangle p(T)\mathcal{G}^-]$

A. Scattering in YZ and ZY polarizations

The Green's functions required for the one-magnon cross section have poles for the energy E at $\pm E_1(0)$ and $\pm E_2(0)$, where $E_1(0)$ and $E_2(0)$ are the zone-center magnon energies in Eq. (17). They have the following general form:

$$\langle\langle \chi; \chi^* \rangle\rangle_E = \left[\frac{\Phi_1(E)}{E^2 - E_1^2(0)} + \frac{\Phi_2(E)}{E^2 - E_2^2(0)}\right], \tag{33}$$

where $\Phi_1(E)$ and $\Phi_2(E)$ are the polarization-dependent functions for NiF_2 involving the magneto-optical coupling coefficients, the exchange and anisotropy terms, and the thermal averages

$$\Phi_1(E) = \frac{R}{4}\{(L_1^+ + L_2^+)^2(E + \Omega - \delta) + (L_1^- + L_2^-)^2(-E + \Omega - \delta) + 2(L_1^+ + L_2^+)(L_1^- + L_2^-)(\alpha - \gamma)\},$$

$$\Phi_2(E) = \frac{R}{4}\{(L_1^+ - L_2^+)^2(E + \Omega + \delta) + (L_1^- - L_2^-)^2(-E + \Omega + \delta) + 2(L_1^+ - L_2^+)(L_1^- - L_2^-)(\alpha - \gamma)\}. \tag{34}$$

Here $R = \langle S^z\rangle/2\pi$ and the expressions for $L_1^\pm$ and $L_2^\pm$ are given in Table I.

It follows from Eqs. (31) and (33) that the differential scattering cross section for the off-diagonal polarizations may be written as

$$\left(\frac{d^2h}{d\Omega d\omega_S}\right) = \frac{\mathcal{F}R\pi}{[1 - \exp(-\beta E)]}\left\{\left[\frac{\Phi_1(E)}{2E_1(0)}\right]\{\delta[E - E_1(0)] - \delta[E + E_1(0)]\} + \left[\frac{\Phi_2(E)}{2E_2(0)}\right]\{\delta[E - E_2(0)] - \delta[E + E_2(0)]\}\right\}. \tag{35}$$

Hence the total integrated intensity can be expressed as

$$\left(\frac{dh}{d\Omega}\right) = \left(\frac{dh}{d\Omega}\right)_S + \left(\frac{dh}{d\Omega}\right)_{AS}, \tag{36}$$

where $(dh/d\Omega)_S$ and $(dh/d\Omega)_{AS}$ denote the Stokes and anti-Stokes integrated intensities, respectively. From Eq. (35) the Stokes integrated intensity is given by

$$\left(\frac{dh}{d\Omega}\right)_S = \mathcal{F}R\pi\left\{\left\{\frac{\Phi_1[E_1(0)]}{2E_1(0)}\right\}\{n[E_1(0)]+1\}+\left\{\frac{\Phi_2[E_2(0)]}{2E_2(0)}\right\}\times\{n[E_2(0)]+1\}\right\}, \tag{37}$$

where $n(E)$ is the Bose-Einstein thermal population factor. The first (second) term on the RHS of Eq. (37) represents the integrated intensity for the upper (lower) energy mode. The anti-Stokes integrated intensity is obtained by replacing $\Phi_i[E_i(0)]\{n[E_i(0)]+1\}$ with $\Phi_i[-E_i(0)]n[E_i(0)]$ for $i=1,2$. At $T=0$ we have $(dh/d\Omega)_{AS}=0$, as expected.

The above results depend on the canting angle and are applicable for any combinations of the magneto-optical coupling coefficients. They simplify, in particular, cases and as an example we may consider the scattering in (YZ) polarization when there is linear magneto-optical coupling only (so $G^+=G^-=0$) and assuming $K^-=0$. If we initially approximate by setting the canting angle $\theta=0$, there is no contribution to the scattering from the lower energy mode [since its energy becomes zero and it can be checked that the weighting factor $\Phi_2(E)=0$]. Then the Stokes integrated intensity from the higher energy mode becomes

$$\left(\frac{dh}{d\Omega}\right)_S = \mathcal{F}|K^+|^2\langle S^{z''}\rangle\left\{\left[\frac{\Omega+\alpha-\delta-\gamma}{2E_1(0)}\right]\{n[E_1(0)]+1\}\right\} \tag{38}$$

while the anti-Stokes to Stokes integrated intensity ratio takes the simple exponential form $\exp(-E_1(0)/k_BT)$. By contrast, in the general case, where there may be both linear and quadratic magneto-optical coefficients and $\theta\neq 0$, the anti-Stokes to Stokes integrated intensity ratio for the higher energy mode is

$$\left(\frac{dh}{d\Omega}\right)_{AS}\Big/\left(\frac{dh}{d\Omega}\right)_S = \exp[-E_1(0)/k_BT]\left\{\frac{\Phi_1[-E_1(0)]}{\Phi_1[E_1(0)]}\right\}. \tag{39}$$

The corresponding ratio for the lower frequency mode is obtained from the above expression by interchanging labels 1 and 2.

In Fig. 11 we compare theory and experiment for the one-magnon scattering from the upper branch in (YZ) polarization for different values of the ratio $|G^+/K^+|$. Here we show results for "in-phase scattering," i.e., with $K^-=G^-=0$ as for equivalent sublattices. It is noteworthy that theory curve A, for which $G^+=0$, does not decrease even as the temperature increases to $0.9T_N$. This can be understood from Eq. (38) because the decrease in the sublattice spin average is compensated by the increase in the thermal population factor. In the case of "out-of-phase scattering" the calculated line shapes are not very sensitive to the ratio $|K^-/G^-|$. The experimental data in Fig. 11 show that the integrated intensity has a relatively weak dependence on temperature throughout the experimental range, which is indicative of a nonzero value for $|G^+/K^+|$. The theory curves for the Stokes intensity of the upper branch in NiF_2 are qualitatively similar to those obtained in Ref. 5 for the one-magnon scattering in MnF_2. In Fig. 12 we show results in (YZ) polarization for the temperature dependence of the anti-Stokes to Stokes intensity ratio for the lower energy branch. The theoretical results here are in qualitative agreement with experimental data if we include effects of the magneto-optical coefficient G^-. The theory curves are obtained taking $G^+=K^-=0$.

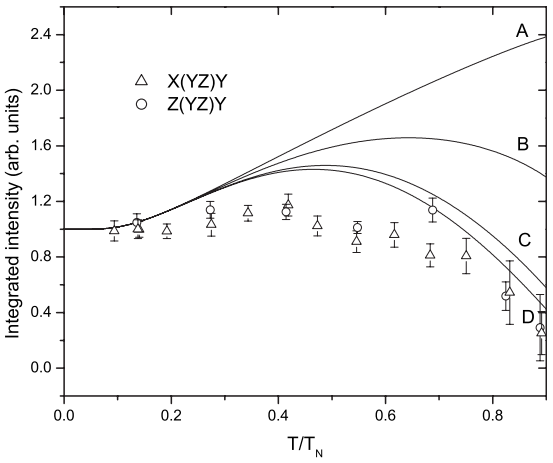

FIG. 11. Comparison of theory and experiment for the temperature dependence of the Stokes integrated intensity for the upper branch in (YZ) polarization. The theory curves are obtained for the following values of $|G^+/K^+|$ A: 0.0, B: 0.1, C: 1, and D: 100.

In Fig. 13 we compare theoretical results between (YZ) and (ZY) polarizations for the integrated intensities of the lower and upper branches. We choose the smallest set of magneto-optical coefficients that lead to qualitative agreement with the experimental data. The overall predicted line shapes are not very sensitive to the choice of K^- and we set its value equal to zero. Similar conclusions are obtained for the (XZ) and (ZX) polarizations. Using the parameter values $|G^+/K^+|=0.0$ and $|G^-/K^+|=0.25$ we can account for the qualitative behavior of the integrated intensity of the lower branch seen in Fig. 2. Experimental data (Fig. 3) have also shown that the integrated intensity of the upper branch in (ZY) polarization is greater than that in (YZ) polarization. Our simplified set of parameters can also account for this feature.

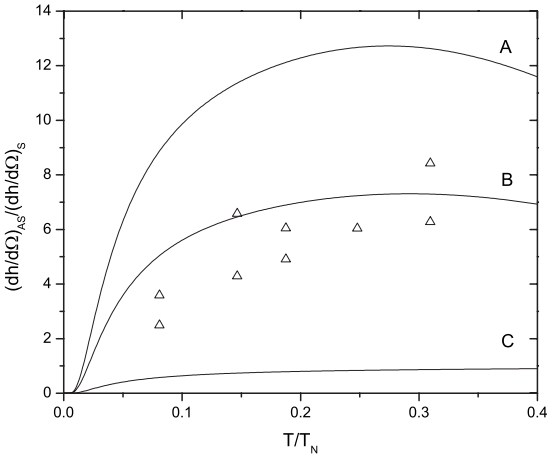

FIG. 12. Comparison of the lower energy branch anti-Stokes to Stokes integrated intensity ratio in (YZ) polarization for different values of $|G^-/K^+|$ A: 0.30, B: 0.25, and C: 0.

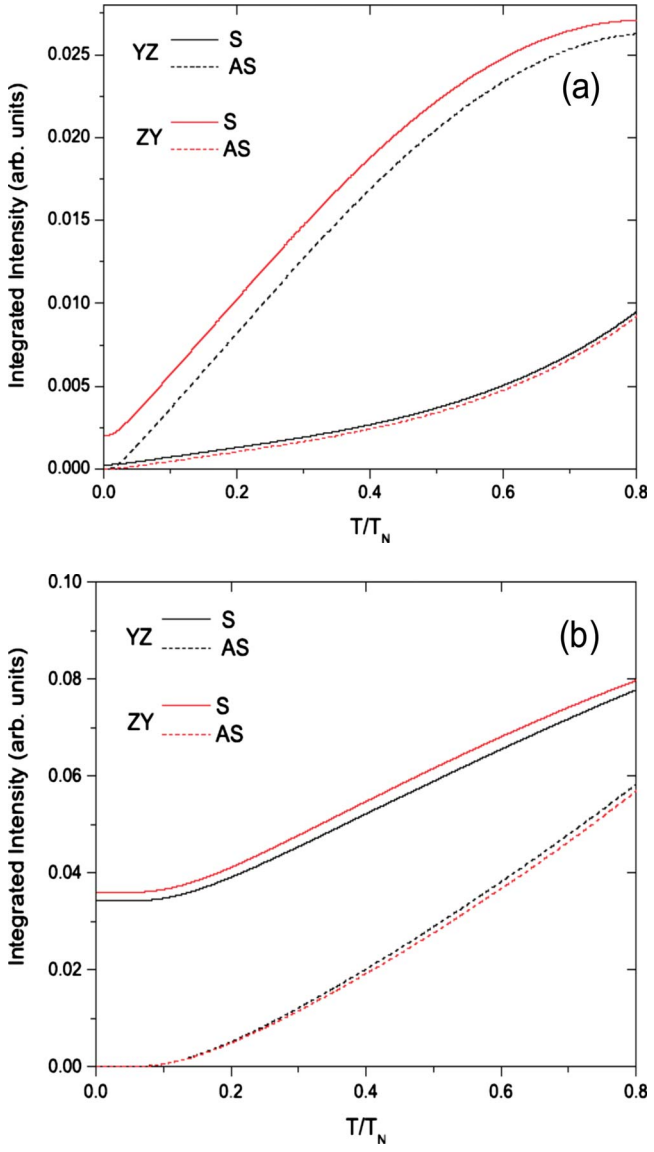

FIG. 13. (Color online) (a) Theory curves for Raman integrated intensities of the lower branch magnons versus temperature in (YZ) and (ZY) polarizations. The Stokes and anti-Stokes curves are denoted by (S) and (AS), respectively. We use the parameter values $K^{-}=0$, $|G^{+}/K^{+}|=0.0$, and $|G^{-}/K^{+}|=0.25$. (b) As in (a) but for the upper branch.

B. Scattering in YX polarization

We now calculate the cross section for the off-diagonal (YX) polarization using a similar approach. The results can again be formally written as in Eq. (35), provided the parameters $L_1^{\pm}$ and $L_2^{\pm}$ are redefined as

$$L_1^{\pm} = \pm K_3 - G_3 \sin(2\theta)\langle S^z\rangle p(T),$$

$$L_2^{\pm} = \mp K_3 - G_3 \sin(2\theta)\langle S^z\rangle p(T). \tag{40}$$

When we substitute Eq. (40) into the expression for $\Phi_1(E)$ we find that the terms proportional to the linear magneto-optical coefficient K_3 vanish. However, the terms involving

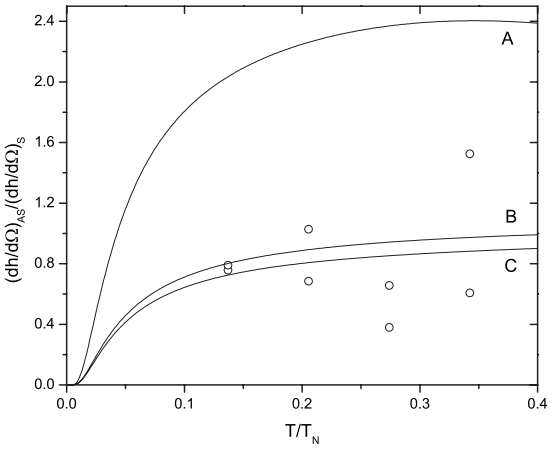

FIG. 14. Comparison of theory with experiment for the temperature dependence of the lower energy branch anti-Stokes to Stokes integrated intensity ratio in (YX) polarization. The theory curves correspond to $|G_3/K_3|$ A: 1.0, B: 0.1, and C: 0.0.

K_3 in $\Phi_2(E)$ do not vanish. Furthermore, if we set $G_3=0$ the Stokes differential cross section reduces to

$$\left(\frac{d^2h}{d\Omega d\omega_S}\right)_{YX} = \frac{\mathcal{F}|K_3|^2\langle S^z\rangle}{[1-\exp(-\beta E)]}\left[\frac{\Omega+\delta-\alpha-\gamma}{2E_2(0)}\right]\delta[E-E_2(0)] \tag{41}$$

and the contribution to the integrated intensity due to the upper branch vanishes. When the quadratic magneto-optical coefficient G_3 is included, it is found that the intensity contribution due to the upper branch is quadratic in θ and may be neglected because of the small canting angle in NiF_2. It is interesting to note that the upper branch was not observed experimentally in the spectra recorded in (YX) polarization.

Finally, in Fig. 14 we plot the calculated anti-Stokes to Stokes integrated intensity ratio in (YX) polarization for the lower branch and we compare with experimental data. We show theory curves for different values of relative magneto-optical coupling coefficients. We find qualitative agreement between theory and experiment when $|G_3|$ is small compared to $|K_3|$. Qualitatively similar results are obtained in the case of (XY) polarization.

V. CONCLUSIONS

Extensive new results from a temperature and polarization-dependent study of the upper and lower branch one-magnon Raman light scattering in the canted antiferromagnet NiF_2 are reported over the temperature range 5–65 K. A comparison between theory and experiment for the frequencies of the one-magnon branches exhibits good agreement for temperatures up to $\sim 0.4T_N$ for the upper branch and up to $\sim 0.2T_N$ for the lower branch. A theoretical model that includes the effects of linear and quadratic magneto-optical coupling is used to account for the observed polarization characteristics of the Stokes and anti-Stokes Raman peaks. By comparing the temperature dependence of the integrated intensities for the lower and upper branches we were able to deduce relative magnitudes of the magneto-optical coeffi-

cients. In many polarizations the quadratic magneto-optical coefficients play a significant role in determining the strength of the scattering intensity. The temperature dependence of the frequency data, together with a lack of agreement with theoretical predictions, for the lower branch magnon is indicative of a spin-reorientation transition at 31 K. We estimate that the spin reorientation in the *a*-*b* crystal plane is on the order of 0.04°. We expect that the overall antiferromagnetic two-sublattice structure remains largely unchanged in the spin reorientation since no jump was observed in the temperature dependence of the upper branch frequency. Further insight into the spin reorientation reported in this work could be obtained by investigating the temperature dependence of the lower frequency magnon branch in the presence of an external magnetic field.

ACKNOWLEDGMENTS

This work was partially supported by the Natural Sciences and Engineering Research Council of Canada (NSERC). We thank G. Wilson for assistance in the Raman spectra analysis and H. J. Labbé for the sample preparation and technical assistance in the NiF_2 Raman measurements.

*Present address: 7801 Computer Ave., Bloomington, MN 55435; eric.meloche@seagate.com

†Present address: B. I. Verkin Institute for Low Temperature Physics, National Academy of Sciences of Ukraine, 61103 Kharkov, Ukraine.

[1] E. Meloche, M. G. Cottam, and D. J. Lockwood, Phys. Rev. B **76**, 104406 (2007).

[2] M. G. Cottam and D. J. Lockwood, *Light Scattering in Magnetic Solids* (Wiley, New York, 1986).

[3] M. T. Hutchings, M. F. Thorpe, R. J. Birgeneau, P. A. Fleury, and H. J. Guggenheim, Phys. Rev. B **2**, 1362 (1970).

[4] P. L. Richards, Phys. Rev. **138**, A1769 (1965).

[5] D. J. Lockwood and M. G. Cottam, Phys. Rev. B **35**, 1973 (1987).

[6] D. J. Lockwood, M. G. Cottam, V. C. Y. So, and R. S. Katiyar, J. Phys. C **17**, 6009 (1984).

[7] A. Latiff Awang and M. G. Cottam, J. Phys. C **12**, 121 (1979).

[8] F. B. Anderson and H. B. Callen, Phys. Rev. **136**, A1068 (1964).

[9] T. Moriya, J. Phys. Soc. Jpn. **23**, 490 (1967).

[10] R. Loudon, J. Phys. C **3**, 872 (1970).

[11] M. G. Cottam, J. Phys. C **8**, 1933 (1975).

[12] http://www.aspiresoftwareintl.com/html/peakfit.html

[13] P. A. Fleury, Phys. Rev. **180**, 591 (1969); Int. J. Magn. **1**, 75 (1970); *Light Scattering in Solids*, edited by M. Balkanski (Flammarion, Paris, 1971), p. 151; P. A. Fleury, R. Loudon, and L. R. Walker, J. Appl. Phys. **42**, 1649 (1971).

[14] D.-M. Hwang, T. T. Chen, and H. Chang, Solid State Commun. **18**, 1099 (1976).

[15] S. M. Rezende and E. F. da Silva, Phys. Rev. B **31**, 570 (1985).

[16] M. E. Lines, Phys. Rev. **156**, 534 (1967).

[17] L. T. Tsymbal and Ya. B. Bazaliy, J. Appl. Phys. **101**, 123919 (2007).

[18] W. Wettling, M. G. Cottam, and J. R. Sandercock, J. Phys. C **8**, 211 (1975).